

A blowout numerical model for the supernova remnant G352.7–0.1

J. C. Toledo-Roy,¹★ P. F. Velázquez,¹★ A. Esquivel¹★ and E. Giacani^{2,3}★

¹*Instituto de Ciencias Nucleares, Universidad Nacional Autónoma de México, Ap.P. 70–543, 04510 DF, Mexico*

²*Instituto de Astronomía y Física del Espacio (CONICET-UBA), CC 67, Suc. 28, 1428 Buenos Aires, Argentina*

³*FADU, University of Buenos Aires, Buenos Aires, Argentina*

Accepted 2013 October 9. Received 2013 October 8; in original form 2013 April 25

ABSTRACT

We present 3D hydrodynamical simulations of the Galactic supernova remnant G352.7–0.1. This remnant is peculiar for having a shell-like inner ring structure and an outer arc in radio observations. In our model, the supernova explosion producing the remnant occurs inside and near the border of a spherical cloud with a density higher than that of the surrounding interstellar medium. A blowout is produced when the remnant reaches the border of the cloud. We have then used the results of our hydrodynamical simulations to calculate synthetic synchrotron radio emission maps, as well as synthetic X-ray maps. For some combinations of the particle acceleration mechanism and the direction of the line of sight, our radio maps display the peculiar morphology of G352.7–0.1 and reproduce the correct relative sizes of the main observed features. At the same time, the calculated X-ray maps reproduce the centrally peaked morphology of the observations.

Key words: hydrodynamics – radiation mechanisms: non-thermal – methods: numerical – ISM: supernova remnants – radio continuum: ISM.

1 INTRODUCTION

Most supernova remnants (SNRs) exhibit a ring-like, limb-brightened morphology in radio frequencies. The spectral index α (defined by $S \propto \nu^{-\alpha}$) of the radio emission is typically in the range 0.5–0.6, indicating that the radio emission is non-thermal, having a synchrotron origin. Such *shell-like* appearance is the traditional picture of an SNR.

However, not all shell-type radio remnants consist of a single well-defined and clearly recognizable ring-like structure. Observations at increasingly higher angular resolution and sensitivity have shown that SNRs exhibit a wide variety of complex morphologies: breakouts, barrel-shaped structures, multiple or incomplete shells, etc. Some examples of this variety include SN 1006 (Kesteven & Caswell 1987), G296.5+10.0 (Giacani et al. 2000), 3C400.2 (Dubner et al. 1994) and Kes 79 (Giacani et al. 2009). Such a diversity reflects not only variations in the properties of the progenitor star and of the explosion itself, but also of the physical conditions of the surrounding interstellar medium (ISM).

The Galactic SNR G352.7–0.1 is an example of a radio SNR with multiple ring structures. Initially identified as an SNR by Clark (1973), its apparent double-ring structure was first noted by Caswell et al. (1983), and was later confirmed by Dubner et al. (1993) by

means of higher angular resolution VLA imaging at 1465 MHz. The most detailed image of G352.7–0.1 available up to the present is that obtained from VLA data at 5 GHz by Giacani et al. (2009) and shown in Fig. 1 as the green channel. As can be seen from this figure, the remnant can be described as an almost complete ring-like structure and a distinct arc-like structure. The smaller ring structure, located to the north-east, is nearly complete and somewhat elliptical, with apparent dimensions of about 4.6×3.5 arcmin². On the other hand, the larger structure to the south-west appears as an arc which subtends an angle of roughly 90° and is located at a distance of about 3.4 arcmin from the apparent centre of the first structure.

The distance to G352.7–0.1 has been estimated by Giacani et al. (2009) through absorption techniques using the H I profiles extracted from the Southern Galactic Plane Survey and applying the Galactic circular rotation model of Fich, Blitz & Stark (1989). They find that the true value probably lies between ~ 6.8 and ~ 8.4 kpc, and conclude that a value of 7.5 ± 0.5 kpc is an adequate estimate of the distance to this remnant. G352.7–0.1 is considered to be a middle-age remnant, with an age, which was estimated from the properties of the X-ray-emitting plasma observed by *XMM-Newton*, of 4700 yr.

From the morphology and spectral properties of G352.7–0.1, Giacani et al. (2009) classify it as belonging to the *mixed-morphology* group due to the combination of the shell-like radio appearance and centre-filled X-ray morphology, which was made evident by the high-resolution observations of *XMM-Newton* (shown as the red channel in Fig. 1). However, the double-ring structure, and notably the south-west arc, has not yet been fully explained. Giacani

* E-mail: juan.toledo@nucleares.unam.mx (JCT-R); pablo@nucleares.unam.mx (PFV); esquivel@nucleares.unam.mx (AE); egiacani@iafe.uba.ar (EG)

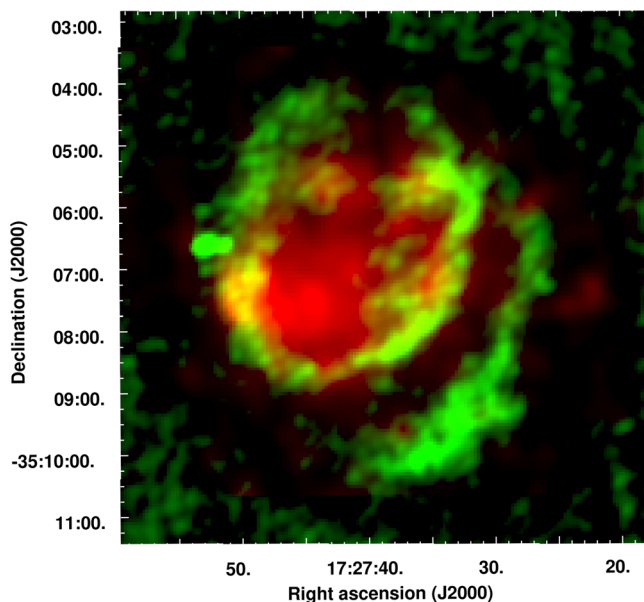


Figure 1. Composite image of G352.7–0.1 obtained from radio observations at 5 GHz (green channel) and X-ray data from *XMM–Newton* (red channel).

et al. (2009) attribute this peculiar morphology to a barrel-shaped structure in the circumstellar medium resulting from an earlier biconic flow expelled from the progenitor (see Manchester 1987, for a more complete discussion of this model). This argument is especially compelling when a pulsar is detected at or near the deduced vertex of the biconic flow. However, no pulsar is known to exist in the interior of G352.7–0.1.

An important idea that has been advanced in order to explain the bilateral nature of some SNRs is that the morphology of the synchrotron emission can depend on the relative orientation of the line of sight with respect to the magnetic field (the aspect angle). For instance, Fulbright & Reynolds (1990) showed that bilateral morphologies are produced for a range of values of the aspect angle.

One crucial aspect involved in the production of asymmetric radio emission in this model is the efficiency of the particle acceleration mechanism responsible for the synchrotron emission behind the SN shock front. The key idea is that the particle injection efficiency depends on the angle between the normal of the shock and the direction of the local magnetic field (the so-called obliquity angle). This dependence can play a determining role in shaping the overall radio morphology of the remnant, especially for bilateral remnants. However, there is still no definite consensus in the literature about which of two particle acceleration mechanisms is dominant, if any. While some studies (e.g. Orlando et al. 2007; Petruk et al. 2009; Schneider et al. 2010) have suggested that the so-called quasi-perpendicular particle injection produces better results, other theoretical and observational studies (e.g. Rothenflug et al. 2004; Bocchino et al. 2011; Petruk et al. 2011; Reynoso, Hughes & Moffett 2013) have found that the quasi-parallel mechanism is more adequate in reproducing observed morphologies in SNRs. The bottom line is that, at this juncture, it is difficult to take one side or the other, or even to assert with certainty whether synchrotron morphology is sensitive to the obliquity angle at all. Therefore, any study that compares synthetic synchrotron emission with the observations should consider both possibilities.

Recently, models of bilateral SNRs have explored aspects that might explain additional details of the asymmetry. For instance,

Orlando et al. (2007) performed 3D numerical simulations of SNR shocks propagating through a magnetized ISM, and studied two specific scenarios: in the first, the remnant expands into a density gradient in the ISM, while in the second the medium has homogeneous density, but the magnetic field strength exhibits a gradient. They found that these gradients in the properties of the ISM can produce bilateral SNRs with limbs of different brightnesses when the line of sight is tilted with respect to the direction of the magnetic field and to the gradients of density or magnetic field strength.

A similar model was applied by Schneider et al. (2010) to explain the asymmetric morphology of SN 1006 in radio continuum and the existence of a filament observed in thermal X-ray emission. In their model, an expanding SNR encounters a density discontinuity in the form of a flat cloud. They obtain synchrotron emission morphologies similar to the observations. Their results depend on the orientation of the interstellar magnetic field relative to the line joining the remnant and cloud centres.

The paper is organized as follows. In Section 2, we explain the blowout model we propose to explain the morphology of G352.7–0.1, with the details of the numerical simulations given in Section 3. Section 4 presents the results of our simulations and corresponding synthetic maps, and discusses their agreement with the observed morphology. Finally, in Section 5, we give our conclusions.

2 THE BLOWOUT MODEL

In our model, we propose that G352.7–0.1 is the result of an SN explosion occurring near the border of a dense spherical cloud, producing a blowout into a lower density surrounding medium. This is similar to the model suggested by Wilner, Reynolds & Moffett (1998) for the case of the remnant 3C 391. We then explore the impact of the different particle injection mechanisms (of electrons behind the shock front) on the resulting asymmetry of the synchrotron morphologies. We seek to reproduce the general morphology of the X-ray emission as well.

With these ideas in mind, we intend to recover the radio morphology of G352.7–0.1, as shown in Fig. 1, as follows: an SN explosion occurs a few pc from the edge of a large spherical cloud, which is denser than, but in pressure equilibrium with, its surrounding medium (see Fig. 2). As the SNR expands and reaches the cloud boundary, it blows out into the lower density ambient medium. Because of the lower density, the remnant expands faster in this medium than it does inside the cloud, and the density behind the shock does not increase as much as it does inside the cloud. As we will see, the north-eastern inner ring-like structure observed in the radio maps can be identified as resulting from the dense ring of material that forms at the cloud–ISM interface. The fact that it is noticeably elliptical in the observations can be explained by a projection effect when the structure is seen at an angle with respect to the line of sight. The second, outer arc located to the south-west is then identified as the part of the remnant that remains inside the cloud, producing an arc-like feature.

An important consideration is the choice of the direction of the ambient magnetic field (assumed initially uniform throughout the domain). Since both the cloud and the SNR are spherical, the initial orientation of the magnetic field (which is dynamically unimportant) is determined solely by the angle it forms with the line joining the centres of the SNR and the cloud (which are aligned with the z -axis; see Fig. 2 for reference). In order to sample a wide range of possibilities, in this work, we have studied the two extreme cases for the direction of the magnetic field: (a) the magnetic field

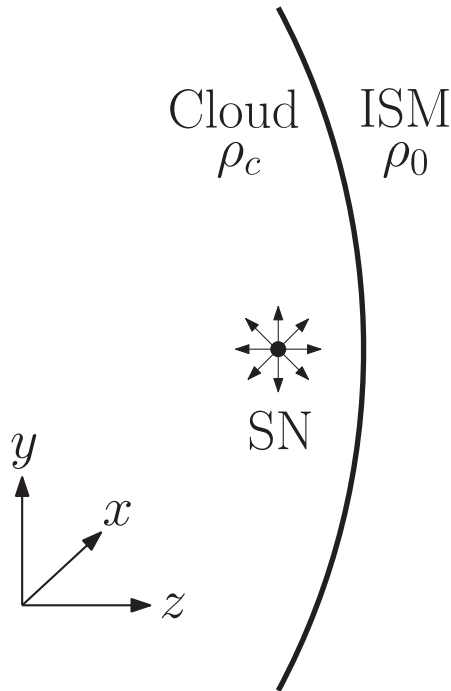


Figure 2. Schematic diagram of the initial conditions of the numerical model. The SN explosion and the centre of the cloud are aligned along the z -axis, while the magnetic field is either oriented along the y -axis or parallel to the z -axis.

aligned with the SNR and cloud centres; and (b) the magnetic field perpendicular to this line. Note that full axial symmetry is present only in the first case (magnetic field parallel to the lines of centres). For any other orientation, axial symmetry is broken by the magnetic field and the simulation must be performed in 3D. Because some aspects of the flow (such as instabilities) can be sensitive to the number of dimensions in which the hydrodynamics is solved, we choose to perform all simulations in 3D so that they can be compared to one another. This has the added benefit that synthetic emission maps are free of artefacts introduced by the axial symmetry during the reconstruction process from 2D axisymmetric data to 3D data.

3 NUMERICAL SIMULATIONS

3.1 Numerical method

The numerical simulations were obtained with the new `WALICXE3D` adaptive mesh refinement 3D hydrodynamical code developed by J. C. Toledo-Roy, which was tested extensively on a distributed-memory cluster. It was developed as a successor and an extension into 3D of the hydrodynamical code `WALICXE` (Esquivel et al. 2010), sharing the overall design philosophy and implementing revised algorithms for adaptive mesh refinement, parallelization and output visualization.

The code solves the gas dynamics equations, which can be written in conservation form as

$$\frac{\partial \rho}{\partial t} + \nabla \cdot (\rho \mathbf{u}) = 0, \quad (1)$$

$$\frac{\partial \rho \mathbf{u}}{\partial t} + \nabla \cdot (\rho \mathbf{u} \mathbf{u}) + \nabla P = 0, \quad (2)$$

$$\frac{\partial E}{\partial t} + \nabla \cdot (\mathbf{u}(E + P)) = -n^2 \Lambda(T), \quad (3)$$

where ρ is the mass density, \mathbf{u} is the fluid velocity and P is the gas pressure. The total energy density E is given by

$$E \equiv \epsilon + \frac{1}{2} \rho |\mathbf{u}|^2, \quad (4)$$

where the internal energy ϵ is related to the gas pressure through the ideal gas equation of state, $\epsilon = P/(\gamma - 1)$.

To solve the gas dynamics equations, the code employs a finite-volume, conservative, second-order Godunov upwind scheme. The Riemann solver uses a second-order Runge–Kutta method for the time integration and a linear spatial reconstruction of the primitive variables at the interfaces, including a slope limiter in order to avoid spurious oscillations. The numerical fluxes are calculated using the HLLC solver, which is a contact discontinuity-capturing modification by Toro, Spruces & Speares (1994) of the original HLL solver (Harten, Lax & van Leer 1983). Because the cooling region behind the main shock cannot be resolved at typical grid resolutions, the code does not limit the integration time-step to the cooling time-scale, employing only the dynamical time-scale (through the standard Courant–Friedrichs–Lewis condition) to limit the time-step size.

For specific details of the code, such as those related to the numerical integrator, the adaptive mesh algorithm or the parallelization scheme, see the appendix of Esquivel et al. (2010), where the precursor 2D version of `WALICXE3D` is described.

Our intention is to compute synthetic synchrotron emission maps from the simulation data, so it is crucial to track the direction of the magnetic field behind the SN shock as the remnant sweeps through the interstellar magnetic field. In order to achieve this, we have included the magnetic field vector as an additional conserved variable and solved at each time-step the induction equation, which can be written in conservation form as

$$\frac{\partial \mathbf{B}}{\partial t} + \nabla \cdot (\mathbf{B} \mathbf{v} - \mathbf{v} \mathbf{B}) = 0. \quad (5)$$

Note that we do not include the back reaction of the magnetic field into the dynamics of the flow [i.e. we do not solve the full magnetohydrodynamics (MHD) equations]. This is justified by the fact that the ambient magnetic field in our simulations is weak and is therefore dynamically unimportant to the evolution of the remnant (the gas pressure is much larger than the magnetic pressure).

It is important to mention that our simplified treatment of the magnetic field may have an impact on the behaviour of hydrodynamic instabilities at the contact discontinuity, which in turn can affect the mixing region in the remnant's interior and thus change the X-ray emission produced therein. However, one of the aims of the paper is to distinguish between a centrally peaked and a ring-like X-ray morphology, as this is one of the principal qualitative elements in the classification of SNRs. The X-ray emission is determined by a combination of the temperature and density distributions in the remnant, and while a full MHD treatment might change the inner structure of the remnant, we do not expect this to be significant enough to reverse the X-ray morphology from a ring-like to a centrally peaked one (see the discussion in Section 4 for further considerations on the validity of our X-ray results regarding this concern).

We simulated a gas with an adiabatic index of $\gamma = 5/3$, neglecting the effects that very efficient particle acceleration may have on the hydrodynamics. Such effects are manifested, for instance, in a smaller distance between the forward shock and the contact

discontinuity (Miceli et al. 2009; Petruk et al. 2011). One way to reproduce the effect of shock modification caused by efficient particle acceleration is to lower the effective adiabatic index of the gas in the simulations to $\gamma \sim 1.1$. However, Orlando et al. (2011) found that the modified γ value mainly has an impact on the absolute values of the non-thermal emission, but not on the large-scale morphology of the remnant. Since our aim is to study the morphological features of the synthetic emission and not to calculate physical absolute values, we use a value of $\gamma = 5/3$.

The code also includes radiative cooling as a source term in the energy equation, equation (3), in which $\Lambda(T)$ is a parametrized cooling function and n is the gas number density. The cooling function $\Lambda(T)$ is taken as a tabulated coronal equilibrium curve (Dalgarno & McCray 1972), which is plotted in fig. 2 of Toledo-Roy et al. (2009). This cooling function is well suited for temperatures above 10^4 K. It is turned off below this threshold, and is substituted by a $\Lambda \propto T^{1/2}$ law (corresponding to the free–free regime) above 10^8 K.

3.2 Initial conditions

The computational domain, spanning a box of $20 \times 20 \times 20$ pc in size, is initialized with a single root block containing 16^3 cells, which is then allowed to refine according to the code’s refinement rules up to six levels of refinement, producing an equivalent resolution at the finest level of 512^3 in a fixed grid.

The simulation box is initially filled with a two-phase pre-existing medium. A spherical cloud having a radius of 30 pc is created with its centre located outside the computational box at the virtual position (10, 10, –18) pc. The cloud has a density of 10 cm^{-3} , a temperature of 10^3 K and is composed of a neutral mixture of 90 per cent hydrogen and 10 per cent helium (yielding a mean atomic mass of $\mu = 1.3$ amu). In the region outside the cloud, the uniform medium has the same chemical composition, a lower number density of 1.0 cm^{-3} and a temperature of 10^4 K. These choices of density and temperature for the two media mean that they are in pressure equilibrium.

The interstellar magnetic field is initially uniform, having a strength of $1 \mu\text{G}$ and a direction either aligned with the y -axis or aligned with the z -axis. This magnetic field is weak enough to be dynamically unimportant, as can be verified by computing the thermal-to-magnetic pressure ratio $\beta \equiv nkT/(B^2/8\pi)$, which has a value of $\beta \sim 35$ for the parameters of our simulations.

At $t = 0$, the remnant of an SN explosion is imposed at (10, 10, 10) pc by injecting 2.0×10^{50} erg of thermal and kinetic energy in equal quantities into a spherical region of radius 0.5 pc, containing an ejecta mass of $2 M_{\odot}$. The radius of this region was chosen to be small enough so that the explosion can be considered almost a point explosion relative to the size of the computational domain, while at the same time being large enough to ensure it is roughly spherical, given the Cartesian discretization of the grid.

In order to validate the correctness of the numerical simulation, we have calculated the radius of the remnant’s main shock as a function of time, for the part of the remnant that remains within the cloud. The result is plotted in Fig. 3. We see that the evolution is initially consistent with the Sedov–Taylor phase ($R \propto t^{2/5}$), until $t_{\text{tr}} \approx 5\text{--}6$ kyr, at which point the slope changes and gradually approaches $R \propto t^{-1/4}$ as the simulation evolves. By comparing the cooling time of the gas behind the shock with the age of the remnant, assuming a simple form for the cooling function, Blondin et al. (1998) obtain that the transition time to the radiative phase should occur at about $t_{\text{tr}} \approx 2.9 \times 10^4 E_{51}^{4/17} n_0^{-9/17}$ yr. With the values in our

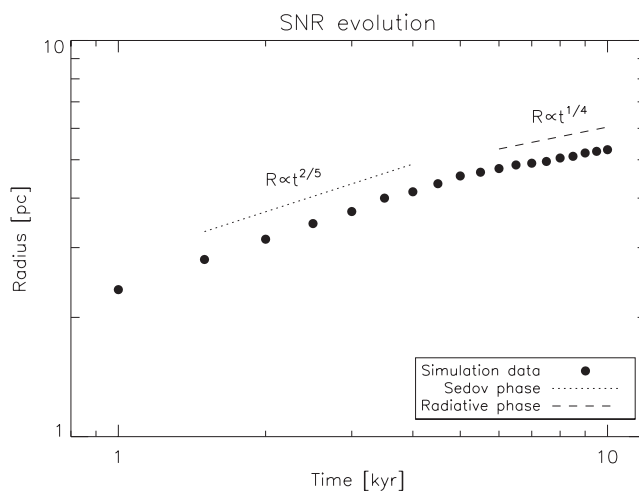


Figure 3. Logarithmic scale plot of the radius of the remnant’s principal shock versus time. The slopes corresponding to the Sedov–Taylor and radiative phases are shown as the dashed lines for comparison.

simulation, we get $t_{\text{tr}} \approx 6$ kyr, which is in agreement with the value we find. It is interesting to note that the part of the remnant that remains within the cloud still evolves as predicted by the standard results for a spherical explosion, despite the fact that the remnant has suffered a blowout and is no longer entirely spherically symmetric. This coincides with the findings of Velázquez et al. (2001).

3.3 Calculation of the synchrotron emission

In order to compare the results from the numerical simulations to the observations, we calculated synthetic radio emission maps by integrating, along the line of sight, the radio emissivity given by (see Ginzburg & Syrovatskii 1965)

$$i(\nu) \propto K B_{\perp}^{\alpha+1} \nu^{-\alpha}, \quad (6)$$

with K being the normalization of the electron distribution behind the shock, B_{\perp} the magnetic field component perpendicular to the line of sight, ν the radio frequency and α the synchrotron spectral index, which has a value of 0.6 for this SNR (Dubner et al. 1993).

The normalization factor K can be expected to vary in time to some extent as the remnant evolves and the shock decelerates. A simple way to account for this is to consider that $K \propto v_s^b$, where v_s is the shock velocity. Reynolds (1998) studied the impact of this dependency on shock velocity for the cases $b = 0, 1$ and 2 , and found that the results are similar in all three cases. Orlando et al. (2007) confirm that the value of b does not affect the main features of the synchrotron morphology of SNRs that expand in a uniform ISM, and that it produces slight alterations in the degree of asymmetry when the gradient in ISM density is perpendicular to the line of sight. Thus, for our case, considering that the synchrotron emission is insensitive to changes in the shock velocity is a reasonable approximation, and in this work we have therefore considered that K is constant in time.

However, the efficiency of particle injection behind the SNR shock front can have a systematic dependence on the obliquity angle ϕ_{Bn} between the normal to the shock and the direction of the magnetic field (Schneider et al. 2010), and this dependence can be used to explain the asymmetric, often bilateral, radio morphology of some SNRs. In this respect, there is currently a debate in the literature as to which mechanism dominates particle acceleration. The two main lines of thought defend either the quasi-perpendicular

($\phi_{Bn} \approx 90^\circ$) or the quasi-parallel ($\phi_{Bn} \approx 0^\circ$) mechanism as being the most efficient in accelerating particles at the shock front. The quasi-parallel mechanism is associated with the classical diffusive shock acceleration (Blandford & Eichler 1987), while the quasi-perpendicular one (also called the shock drift mechanism) can become a more efficient process because of particle acceleration by electric fields along the shock front (see e.g. Jokipii 1987).

To explore the range of possibilities regarding this matter, in this work we have calculated synchrotron emission maps for three distinct cases of the injection mechanisms: (1) isotropic (no ϕ_{Bn} dependence), (2) quasi-parallel ($\phi_{Bn} \approx 0^\circ$), and (3) quasi-perpendicular ($\phi_{Bn} \approx 90^\circ$). Following Orlando et al. (2007) and Schneider et al. (2010), we calculate synchrotron emission by using equation (6) and setting the normalization factor of the electron distribution K as a constant in the isotropic case, or being proportional to either $\cos^2\phi_{Bs}$ or $\sin^2\phi_{Bs}$, for the quasi-parallel and quasi-perpendicular cases, respectively, where ϕ_{Bs} is the angle between the shock normal and the direction of the *post-shock* magnetic field. The latter can be related to the obliquity angle ϕ_{Bn} (for strong shocks, which is the case here) through $\cos^2\phi_{Bs} = \cos^2\phi_{Bn}/(16 - 15\cos^2\phi_{Bn})$ (Orlando et al. 2007). Finally, in order to estimate the angle ϕ_{Bn} itself from the numerical results, we estimated the direction of the shock normal using either the direction of the velocity vector (at the shock) or that of the local pressure gradient.

3.4 Calculation of the thermal X-ray emission

In order to further compare the results of the numerical simulations with the observations, we have also calculated synthetic thermal X-ray maps by integrating the X-ray emission coefficient $j_\nu(n, T)$. The coefficient was calculated (in the low-density regime) as $j_\nu(n, T) = n_e^2 \xi(T)$, where n_e and T are the electronic density (taken to be $n_e \approx n$) and temperature obtained from our numerical simulations, while $\xi(T)$ is a function that changes smoothly with temperature. The function $\xi(T)$ was computed for the range 0.15–8 keV and standard solar metallicity using the CHIANTI atomic data base and its associated IDL software (Dere et al. 1997; Landi et al. 2006).

4 RESULTS

The panels of Fig. 4 show a y - z cut of the number density along $x = 10$ pc for four different evolution times. The remnant's main shock collides with the edge of the cloud shortly after 1 kyr. Because the surrounding medium is of lower density, as the main shock blows out of the cloud it accelerates, and the blown-out structure rapidly increases in size. By $t = 5500$ kyr, the remnant has been considerably blown out, resulting in a structure that is 5–6 pc in size (see Fig. 4d). As can be seen from the figure, the post-shock gas density is higher when the shock expands within the cloud than when it expands into the surrounding medium. As we will see, the expanding ring of dense shocked gas produced on the surface of the spherical cloud is key in producing a ring-like radio feature.

In Fig. 5, we show a sample of synthetic synchrotron maps projected into the plane of the sky for the snapshot at $t = 5500$ yr, which is consistent with the approximate age of the remnant within uncertainty factors. The maps are calculated with different combinations of (i) the particle acceleration mechanism used to compute the emission, indicated by the labels ISO (isotropic, no dependence), PAR (quasi-parallel) or PER (quasi-perpendicular); (ii) the orientation of the magnetic field before the line-of-sight rotation, shown as an arrow on the leftmost column; and (iii) the orientation of the line

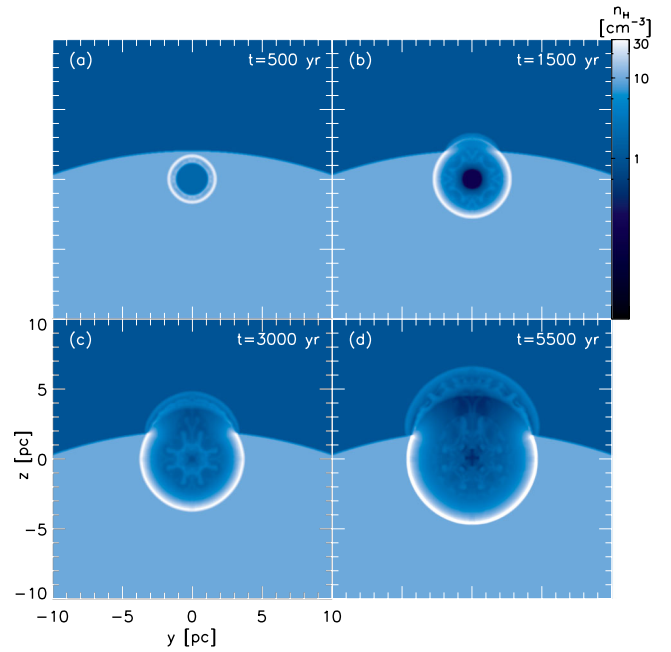


Figure 4. Evolution of the number density (given in cm^{-3}) from the hydrodynamical simulation (cuts in the y - z plane along $x = 10$ pc) corresponding to time snapshots at (a) 1000, (b) 2000, (c) 3500 and (d) 5500 yr. The colour scale and physical sizes of the boxes are the same in all panels.

of sight used for the projection, measured as the angle between the line of sight and the z -axis of the simulation and indicated by the number in degrees in the upper right-hand corner.

The panels in the upper and lower rows of Fig. 5 correspond to the case where the ambient magnetic field is perpendicular to the line joining the centres of the cloud and the SNR. In that case, we find that the isotropic and quasi-perpendicular acceleration models produce the best results when the object is seen with the z -axis tilted about 60° with respect to the plane of the sky (panels b and e). These maps display the main features of G352.7–0.1, namely an ellipsoidal ring-like structure with a larger, incomplete arc. Note that a rotation angle of 60° is approximately that which is required to produce an ellipse with the axial ratio seen in the radio observations (see Fig. 1) from a circular ring.

Because of the geometric dependence of the particle acceleration efficiency on the obliquity angle, we expect that the quasi-parallel mechanism should yield comparable results when the ambient magnetic field is parallel, instead of perpendicular, to the line of centres. The panels d–f of the middle row correspond to this case. We see that when the line of sight is tilted about 60° (panel e), some of the ellipsoidal features of the isotropic or quasi-perpendicular cases are recovered. However, the larger incomplete arc becomes much fainter. It also appears that in the quasi-parallel case our synchrotron synthesis routine yields results that are more sensitive to small-scale structure in the hydrodynamic solution, which is made evident by the noisier appearance of these maps.

We also model the distribution of the X-ray emission from G352.7–0.1. Fig. 6 shows a synthetic X-ray map for $t = 5500$ yr in the range 0.15–8 keV. Interstellar absorption has been included in the calculation, assuming that the column density in the direction to G352.7–0.1 is $2.6 \times 10^{22} \text{ cm}^{-2}$ (Giacani et al. 2009). The most striking qualitative feature is that the emission is approximately central, in close agreement with the X-ray observations of Giacani et al. (2009) (see fig. 10 in that work).

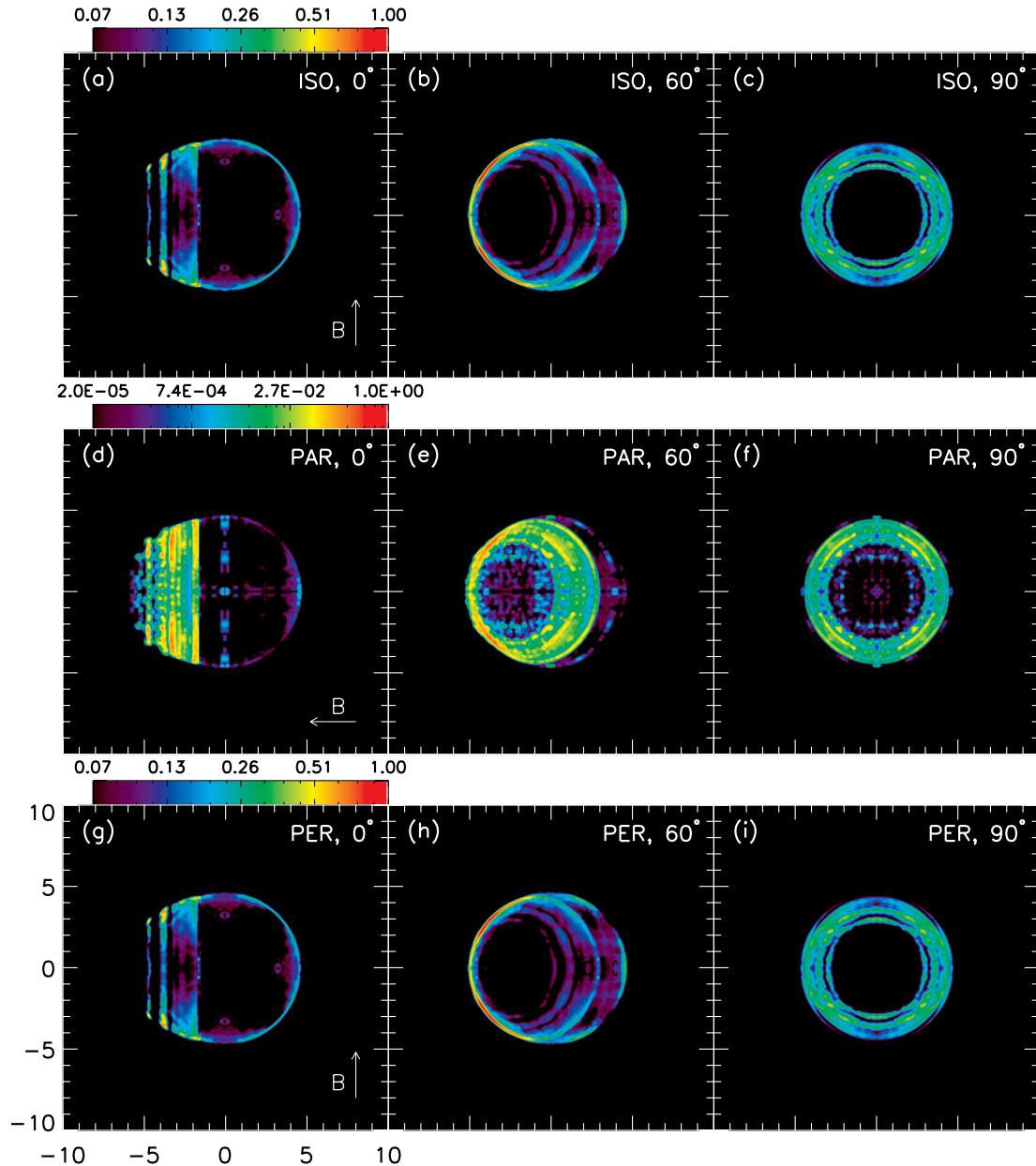


Figure 5. Synthetic synchrotron maps projected into the plane of the sky for three different orientations and for the three acceleration methods. The acceleration methods are indicated in the upper right-hand corner of each panel with the labels PAR (quasi-parallel), PER (quasi-perpendicular) and ISO (isotropic). In the maps of the upper and lower rows, the magnetic field is initially oriented perpendicular to the line of centres, while for the middle row it is oriented parallel to this line. The angular label in each panel indicates the amount of rotation towards the line of sight applied before projection. The colour bars shown are shared by the three subpanels of each row, and are given in units that are normalized to the same maximum value. Note that the scale is logarithmic, and that the middle row has a much wider range than the top or bottom row. The physical size is the same for all panels: 20×20 pc.

Centre-filled X-ray morphologies are generally associated with middle-age remnants. To explain this behaviour, a critical factor is the decrease of the temperature behind the main shock below $\sim 10^6$ K, at which point radiative losses become important and the material behind the shock quickly cools. The result is that the X-ray emission behind the main shock decreases, possibly to a point where the less intense emission from the interior becomes dominant. In our simulations of G352.7–0.1, the remnant is beginning to transition into the radiative phase at $t = 5500$ yr, which puts it in the category of middle-age remnants. Because interstellar absorption will mainly attenuate the limb emission, the inclusion

of absorption in our calculated maps reinforces the centre-bright feature of the emission.

It must also be noted that our simulations do not include the effects of thermal conduction, which has been shown to have an important effect on the thermal X-ray emission when the remnant enters transitions to the radiative phase of evolution (see e.g. Balsara, Tilley & Howk 2008a; Balsara et al. 2008b; Zhou et al. 2011). Our simulated maps correspond to a slightly earlier remnant age, in which the remnant is still in the Sedov phase and only about to start the transition into the radiative one. Moreover, it has been verified that the effect of thermal conduction is to shift the emission

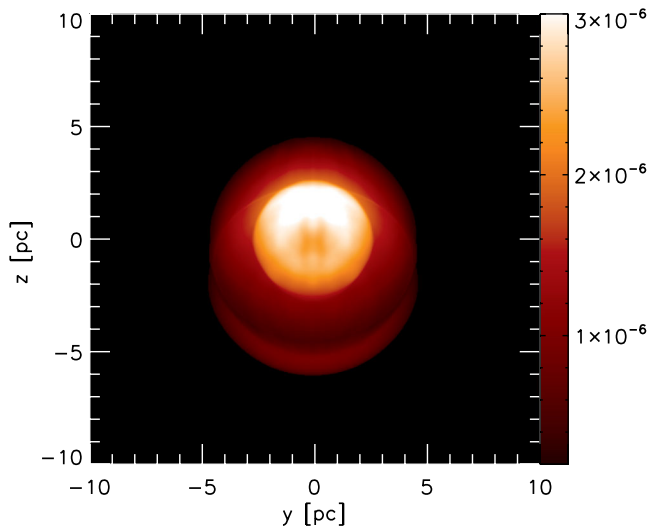


Figure 6. Simulated X-ray map in the range 0.15–8 keV for $t = 5500$ yr. Absorption by a column density of $2.6 \times 10^{22} \text{ cm}^{-2}$ has been included. The indicated colour scale is given in units of $\text{erg s}^{-1} \text{ cm}^{-2} \text{ sr}^{-1}$.

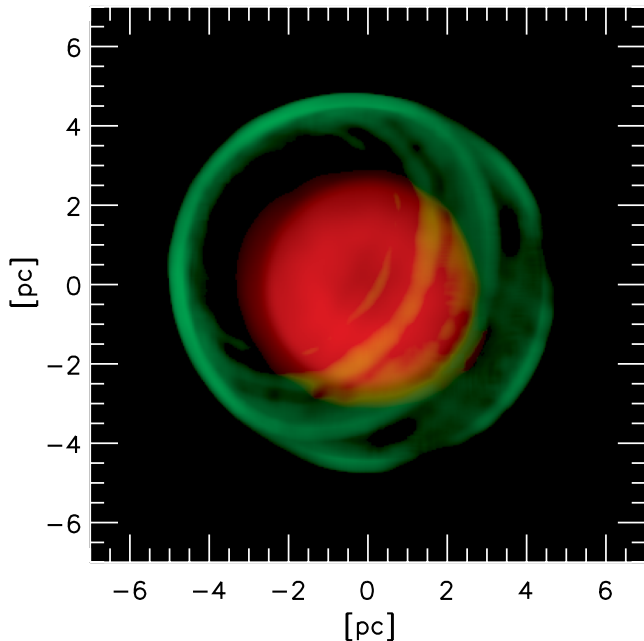


Figure 7. Composite image showing synthetic X-ray emission in the range 0.15–8 keV (red channel) and synthetic synchrotron emission calculated using the quasi-perpendicular mechanism (green channel). The X-ray emission shown here ranges from 8×10^{-7} to $4 \times 10^{-6} \text{ erg s}^{-1} \text{ cm}^{-2} \text{ sr}^{-1}$, while the synchrotron emission ranges from 6×10^8 to 1×10^{10} , in arbitrary units. The images have been smoothed to approximate the beam size employed in the observations.

morphology from ring like to centrally peaked (e.g. Velázquez et al. 2004; Schneider, de La Fuente & Velázquez 2006; Tilley, Balsara & Howk 2006). Thus, we expect that the inclusion of thermal conduction in our simulations would in fact enhance the centrally peaked X-ray morphology obtained.

Finally, in Figs 7 and 8 we show composite images where the calculated X-ray (red channel) and synchrotron (green channel) emissions have been superimposed. In Fig. 7, the synchrotron emission has been calculated using the quasi-perpendicular mechanism,

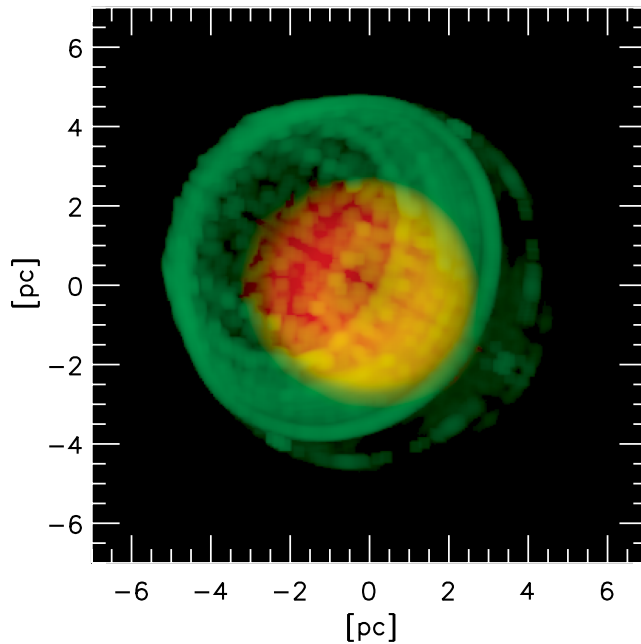


Figure 8. Same as Fig. 7, but with synchrotron emission calculated using the quasi-parallel mechanism.

while in Fig. 8 the quasi-parallel mechanism was used. We oriented the images so that they can be compared directly to the observations (see Fig. 1). We observe that the synchrotron emission exhibits multiple arcs and rings, and that the X-ray emission is roughly contained within the radio structure.

5 CONCLUSIONS

We have explored a blowout scenario to explain the morphological features of the Galactic SNR G352.7–0.1. In our model, the SN explosion occurs inside but near the border of a spherical cloud. The consequence is that the remnant undergoes a considerable blowout into the lower density surrounding medium. The resulting hydrodynamical structure was then used to produce synthetic radio synchrotron and thermal X-ray maps, with the aim of comparing with the available observations.

The obtained synchrotron emission resembles the radio observations of G352.7–0.1 when the line joining the cloud and explosion centres forms an angle of 60° with the plane of the sky. This angle is in close agreement with the angle suggested in radio observations by the axial ratio of the ellipsoidal inner ring-like structure. We have explored the effects of different obliquity angle dependences on the particle acceleration efficiency, and found that both the quasi-perpendicular and quasi-parallel mechanisms can produce multiple ring-like or arc-like structures, noting that in our specific model for G352.7–0.1, the larger incomplete arc is fainter than observed when using the quasi-parallel dependence. However, considering the results of recent numerical studies of other SNRs, we cannot conclude, based on our work, that one of the mechanisms should be generally dominant in this kind of astrophysical objects. An observational determination of the direction of the ambient magnetic field around this remnant, obtained through polarization measurements (such as the one by Reynoso et al. 2013, for SN1006), would certainly help restrict the possibilities.

We would like to emphasize the role played by the particle acceleration efficiency mechanism and the direction of the line of sight in

producing distinct morphologies for SNRs when the spatial structure of the remnant is not spherically symmetric. Both factors are capable to radically change the observed shape and features that are observed. This fact can certainly be exploited to produce simpler and more effective models for many asymmetrical SNRs.

As for the X-ray results, we recover a centre-filled morphology as observed in G352.7–0.1 when the synthetic emission is absorbed through a column density consistent with the value obtained from observations. Because the energy of the explosion is relatively low while the cloud density is higher than the usual ISM value, the transition of the remnant's evolution into the radiative phase occurs slightly after the time-frame of the maps we have presented, thus reinforcing the notion that centre-bright X-ray emission corresponds to middle-age remnants. We expect that including thermal conduction in our simulations would enhance the centrally peaked morphology.

ACKNOWLEDGEMENTS

The authors thank an anonymous referee for insightful and constructive comments that helped improve this study. We also thank Enrique Palacios for maintaining the ‘Diable’ cluster where the simulations were performed. PFV and AE acknowledge support from the CONACyT grants 61547, 101356, 101975, 167611, and UNAM DGAPA grant IN105312. EG is partially supported by grants UBACyT W011, PIP 0736/2012 (CONICET) and PICT-ANPCYT 0571/2011. CHIANTI is a collaborative project involving George Mason University, the University of Michigan (USA) and the University of Cambridge (UK).

REFERENCES

- Balsara D. S., Tilley D. A., Howk J. C., 2008a, *MNRAS*, 386, 627
 Balsara D. S., Bendinelli A. J., Tilley D. A., Massari A. R., Howk J. C., 2008b, *MNRAS*, 386, 642
 Blandford R., Eichler D., 1987, *Phys. Rep.*, 154, 1
 Blondin J. M., Wright E. B., Borkowski K. J., Reynolds S. P., 1998, *ApJ*, 500, 342
 Bocchino F., Orlando S., Miceli M., Petruk O., 2011, *A&A*, 531, A129
 Caswell J. L., Haynes R. F., Milne D. K., Wellington K. J., 1983, *MNRAS*, 203, 595
 Clark D. H., 1973, *Nat*, 246, 28
 Dalgarno A., McCray R. A., 1972, *ARA&A*, 10, 375
 Dere K. P., Landi E., Mason H. E., Monsignori Fossi B. C., Young P. R., 1997, *A&AS*, 125, 149
 Dubner G. M., Moffett D. A., Goss W. M., Winkler P. F., 1993, *AJ*, 105, 2251
 Dubner G. M., Giacani E. B., Goss W. M., Winkler P. F., 1994, *AJ*, 108, 207
 Esquivel A., Raga A. C., Cantó J., Rodríguez-González A., López-Cámara D., Velázquez P. F., De Colle F., 2010, *ApJ*, 725, 1466
 Fich M., Blitz L., Stark A. A., 1989, *ApJ*, 342, 272
 Fulbright M. S., Reynolds S. P., 1990, *ApJ*, 357, 591
 Giacani E. B., Dubner G. M., Green A. J., Goss W. M., Gaensler B. M., 2000, *AJ*, 119, 281
 Giacani E., Smith M. J. S., Dubner G., Loiseau N., Castelletti G., Paron S., 2009, *A&A*, 507, 841
 Ginzburg V. L., Syrovatskii S. I., 1965, *ARA&A*, 3, 297
 Harten A., Lax P. D., van Leer B., 1983, *SIAM Rev.*, 25, 357
 Jokipii J. R., 1987, *ApJ*, 313, 842
 Kesteven M. J., Caswell J. L., 1987, *A&A*, 183, 118
 Landi E., Del Zanna G., Young P. R., Dere K. P., Mason H. E., Landini M., 2006, *A&AS*, 162, 261
 Manchester R. N., 1987, *A&A*, 171, 205
 Miceli M. et al., 2009, *A&A*, 501, 239
 Orlando S., Bocchino F., Reale F., Peres G., Petruk O., 2007, *A&A*, 470, 927
 Orlando S., Petruk O., Bocchino F., Miceli M., 2011, *A&A*, 526, A129
 Petruk O. et al., 2009, *MNRAS*, 393, 1034
 Petruk O., Beshley V., Bocchino F., Miceli M., Orlando S., 2011, *MNRAS*, 413, 1643
 Reynolds S. P., 1998, *ApJ*, 493, 375
 Reynoso E. M., Hughes J. P., Moffett D. A., 2013, *AJ*, 145, 104
 Rothenflug R., Ballet J., Dubner G., Giacani E., Decourchelle A., Ferrando P., 2004, *A&A*, 425, 121
 Schneider E. M., de La Fuente E., Velázquez P. F., 2006, *MNRAS*, 371, 369
 Schneider E. M., Velázquez P. F., Reynoso E. M., de Colle F., 2010, *MNRAS*, 408, 430
 Tilley D. A., Balsara D. S., Howk J. S., 2006, *MNRAS*, 371, 1106
 Toledo-Roy J. C., Velázquez P. F., de Colle F., González R. F., Reynoso E. M., Kurtz S. E., Reyes-Iturbide J., 2009, *MNRAS*, 395, 351
 Toro E. F., Spruces M., Speares W., 1994, *Shock Waves*, 4, 25
 Velázquez P. F., de la Fuente E., Rosado M., Raga A. C., 2001, *A&A*, 377, 1136
 Velázquez P. F., Martinell J. J., Raga A. C., Giacani E. B., 2004, *ApJ*, 601, 885
 Wilner D. J., Reynolds S. P., Moffett D. A., 1998, *ApJ*, 115, 247
 Zhou X., Miceli M., Bocchino F., Orlando S., Chen Y., 2011, *MNRAS*, 415, 244

This paper has been typeset from a $\text{\TeX}/\text{\LaTeX}$ file prepared by the author.